Supplement of The Cryosphere, 16, 3375–3391, 2022
https://doi.org/10.5194/tc-16-3375-2022-supplement

The Cryosphere
Open Access

Supplement of

The impact of climate oscillations on the surface energy budget over the Greenland Ice Sheet in a changing climate

Tiago Silva et al.

Correspondence to: Tiago Silva (tiago.ferreira-da-silva@uni-graz.at)

1 Study Area

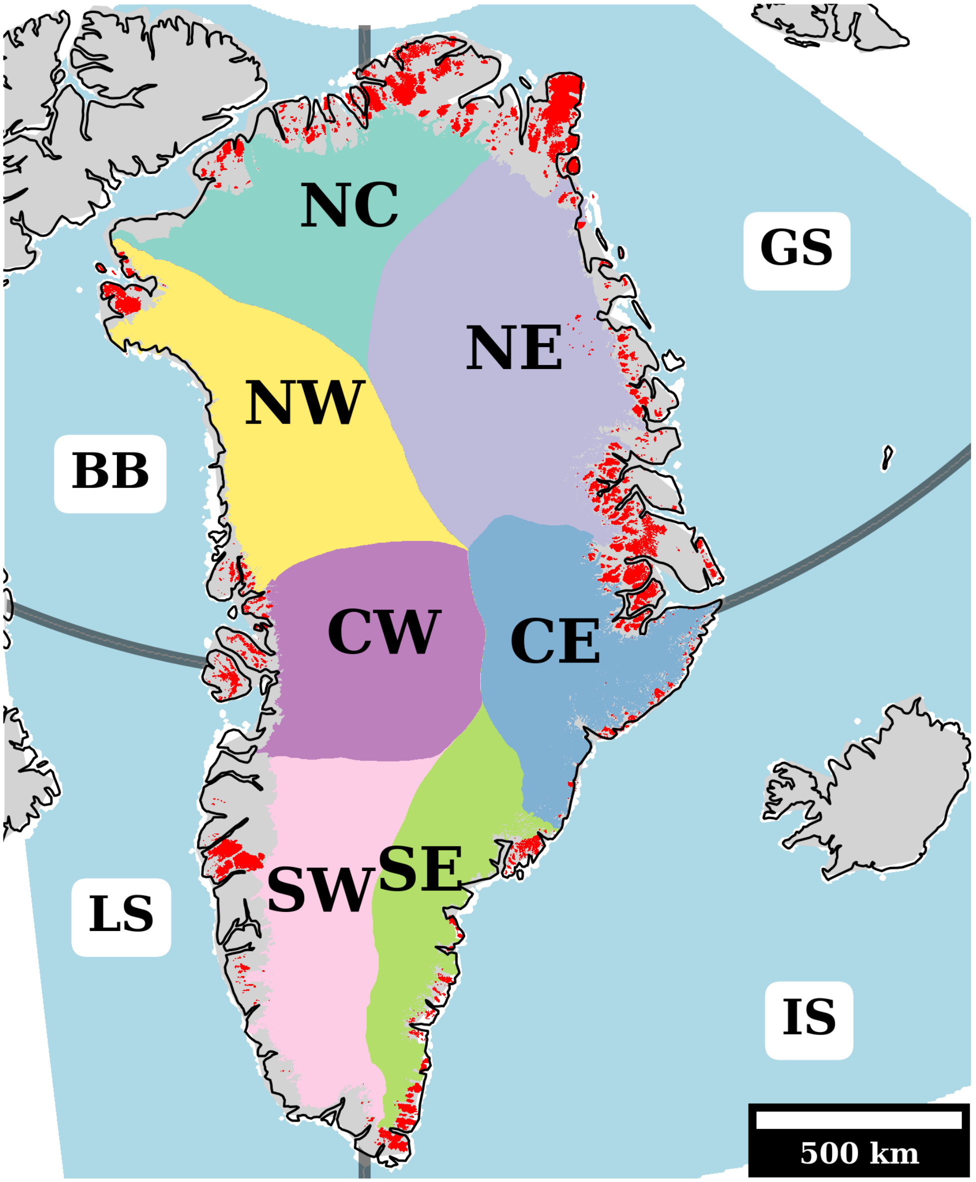

Figure S1. Map of the Greenland ice sheet and peripheral glaciers (in red) separated by main drainage basins. The meridian 45°W and the parallel 70°N are used to divide the adjacent seas (in blue) in four quadrants: Baffin Bay (BB); Labrador Sea (LB); Greenland Sea (GS); and Irminger/Icelandic Sea (IS). The Denmark Strait is situated in between Greenland and Iceland.

2 Trend analysis for summer ablation rate

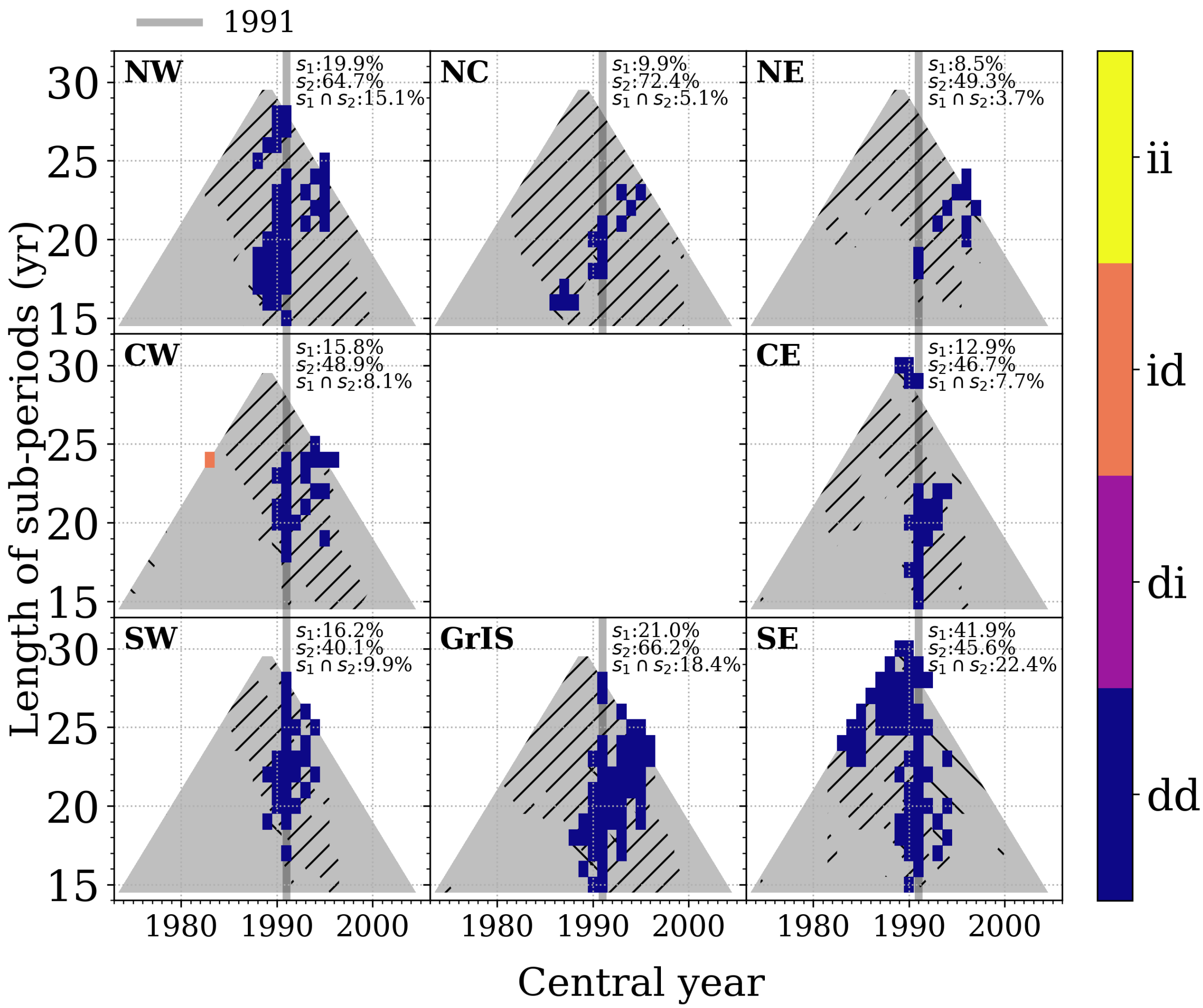

Figure S2. Regional Mann-Kendall (M-K) trend classification by splitting the data-set in two equally-sized sub-periods (y-axis) and varying its time-center (x-axis) for the surface integrated ablation rate in summer from RACMO2 between 1959-2020. Regional M-K trend classification is only shown when both sub-periods show confidence higher than 90%. i(d) stands for increasing(decreasing) trend prior to and subsequent to the central (splitting) year. Significant first (second) sub-period trends are left (right) tilted, whereas the rest is illustrated by the gray shaded area. The upper-right corner indicates the relative frequency of significant sub-periods. For reference, 1991 is marked with a thick line.

Since the late-1980s, the (sub-)period length increases for recent central splitting years in most regions, which indicates high surface mass loss variability among short sub-periods. Moreover, significant surface mass loss trends are more common in recent decades, ranging from 40% in the southwest to 72% (out of all possible sub-period trends - gray shaded area) in north

Greenland. Southeast is the region with more significant trends among periods. Except in the northern part and the northeast, most significant trends are found for the central splitting year of 1990-91 in a wide range of period's lengths and with the highest ratios. Moreover, the performed trend analysis suggests no influence from the Pinatubo eruption in 1992.

3 Climate oscillations

The highest and lowest seasonal 25^{th} percentiles are initially used to identify positive and negative index phases, respectively, and values in between are considered neutral phases. Hence, between 1959 and 2020 each season comprises 16 positive, 16 negative and 30 neutral phases. The seasonal index phase count is uneven when splitting the period in 1991. Spring, summer and autumn GBI comprise more positive phases after 1991, while the opposite is seen in winter. All seasons show more negative GBI phases before 1991 with the opposite identified for NAO. Increasing the percentile threshold would not balance the index phase count before and after 1991, in fact it would approximate the climate oscillation threshold towards zero (e.g. the lowest 30^{th} percentile in SON). Moreover, the impact of climate oscillations with thresholds close to zero is highly variable since distinctions of the prevailing weather pattern among "neutral phases" are unclear. Decreasing the threshold percentile would make the summer sample with one unit size before 1991 (e.g. highest 20^{th} percentile in JJA).

3.1 Clustering Analysis

We performed a sensitivity analysis of the NAG by using two NAO products, more specifically NAO (van den Dool et al., 2000) and (Hurrell et al., 2003). Although both products use the same method to calculate NAO, they differ on the atmospheric level used. NAO calculated by van den Dool et al. (2000) relies on the 500 hPa geopotential height (hereafter NAO500) and Hurrell et al. (2003) depends on surface pressure (hereafter NAOsfc). In addition, we also compare both products for the percentile classification. The corresponding NAG and NAO phase and the associated years are shown in Table S1 and S2. Important to highlight that NAO500 and NAOsfc were standardized before producing NAG and NAO percentiles.

Both, NAG and NAO, present differences in the classification depending on the product used. Relative differences are always smaller for NAG than NAO classifications. In winter (summer), NAG and NAO classifications differ the most under the neutral phase. However, relative changes in 0NAG are below 5% (10%) while for 0NAO are around 25% (22). These differences in 0NAG and 0NAO are related to adjustment and separation with other phases, without changes for contrasting phases. The number of 0NAG in winter is comparable regardless of the NAO used. However, 0NAG in summer using NAO500 aggregates several years.

The relationship between GBI and NAO500 or NAOsfc was also explored within NAG clusters. In winter, NAOsfc correlates better with GBI within NAG clusters than NAO500. In fact, owing to the high variability of the data no connection could be found between NAO500 and GBI within winter clusters. This was also mentioned by Hanna et al. (2018), who used the same product. This serves to point that the influences exerted by NAO and GBI composites at 500 hPa may differ (Fig. S3).

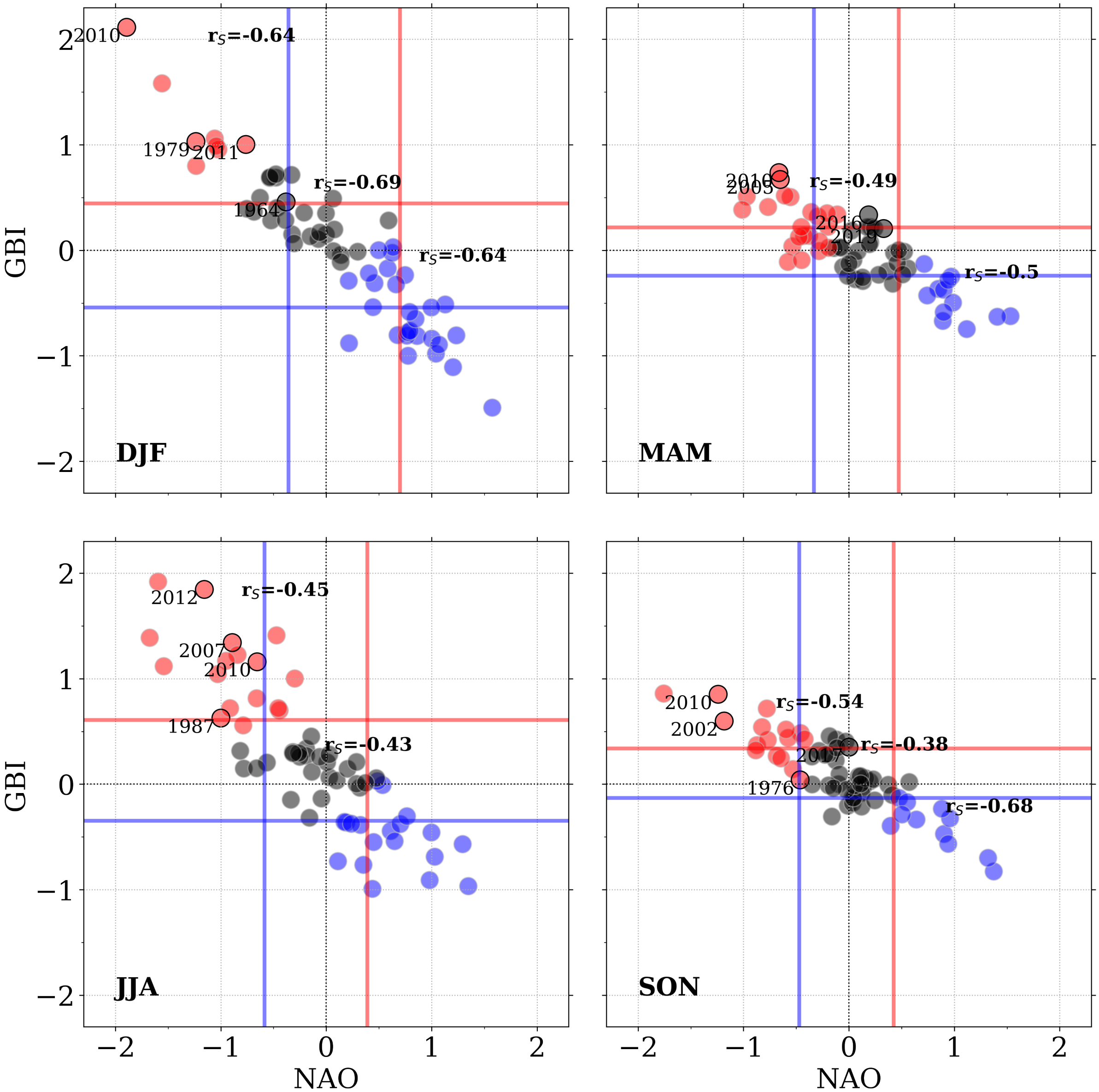

Figure S3. Seasonal NAG phases based on the k-means clustering: positive (red cluster); neutral (black cluster); and negative (blue cluster) phase. NAO and GBI phases are categorized based on the respective seasonal 25th (blue line) and 75th (red line) percentile. The Spearman correlation coefficient (r_S) is shown for clusters with significance higher than 90%. The third-dimension corresponding to GrIS IWV is omitted. The dark circle indicates years whose seasonal GrIS IWV is greater than the 95th percentile.

Table 1. Comparison between NAG and NAO classifications by using NAO from van den Dool et al. (2000) or Hurrell et al. (2003). The number of NAG and NAO phases between 1959-2020 and the corresponding years are indicated. Years that differ depending on the source are highlighted in bold.

DJF	**NAG**	**+**	**0**	**–**
	van den Dool et al. (2000)	8 1960, 1963, **1964**, 1969, 1977, 1979, 2010, 2011	26 1959, 1962, 1965, **1966**, 1967, 1968, 1970, 1971, 1978, 1980, 1982, 1985, 1986, 1987, 1996, 1997, 1998, 2001, 2002, 2003, 2004, 2006, 2007, 2009, 2013, 2019	28 1961, 1972, 1973, 1974, 1975, 1976, 1981, 1983, 1984, **1988**, 1989, 1990, 1991, 1992, 1993, 1994, 1995, 1999, 2000, 2005, 2008, 2012, 2014, 2015, 2016, 2017, 2018, 2020
	Hurrell et al. (2003)	8 1960, 1963, **1966**, 1969, 1977, 1979, 2010, 2011	27 1959, 1962, **1964**, 1965, 1967, 1968, 1970, 1971, 1978, 1980, 1982, 1985, 1986, 1987, **1988**, 1996, 1997, 1998, 2001, 2002, 2003, 2004, 2006, 2007, 2009, 2013, 2019	27 1961, 1972, 1973, 1974, 1975, 1976, 1981, 1983, 1984, 1989, 1990, 1991, 1992, 1993, 1994, 1995, 1999, 2000, 2005, 2008, 2012, 2014, 2015, 2016, 2017, 2018, 2020
	NAO	**–**	**0**	**+**
	van den Dool et al. (2000)	16 1960, 1963, **1964**, 1965, 1966, 1968, 1969, 1970, **1971**, 1977, 1978, 1979, 1985, 1996, 2010, 2011	30 1959, 1961, 1962, 1967, 1972, **1973**, 1974, 1975, **1976**, 1980, 1981, 1982, **1986**, 1987, **1990**, **1992**, 1997, 1998, **1999**, 2001, 2002, 2003, 2004, 2006, 2007, **2008**, 2009, **2013**, 2017, 2019	16 1983, 1984, **1988**, 1989, 1991, 1993, **1994**, 1995, 2000, **2005**, 2012, **2014**, 2015, 2016, **2018**, 2020
	Hurrell et al. (2003)	16 1960, 1963, 1965, 1966, 1968, 1969, 1970, 1977, 1978, 1979, 1985, **1986**, 1996, 2010, 2011, **2013**	30 1959, 1961, 1962, **1964**, 1967, **1971**, 1972, 1974, 1975, 1980, 1981, 1982, 1987, **1988**, **1994**, 1997, 1998, 2001, 2002, 2003, 2004, **2005**, 2006, 2007, 2009, **2014**, 2016, 2017, **2018**, 2019	16 **1973**, **1976**, 1983, 1984, 1989, **1990**, 1991, **1992**, 1993, 1995, **1999**, 2000, **2008**, 2012, 2015, 2020

JJA	NAG	+	0	–
	van den Dool et al. (2000)	16 1960, 1980, 1987, 1993, 1998, 2007, 2008, 2009, 2010, 2011, 2012, 2014, 2015, 2016, 2019, 2020	32 1959, 1962, 1963, 1966, 1968, 1969, 1971, **1973**, 1974, 1975, 1977, 1978, 1981, 1982, 1984, 1985, 1986, **1988**, **1989**, 1990, 1991, 1995, 1997, **1999**, 2000, 2001, 2002, **2003**, 2004, 2005, 2006, **2017**	14 1961, 1964, 1965, 1967, 1970, 1972, 1976, 1979, 1983, 1992, 1994, 1996, 2013, 2018
	Hurrell et al. (2003)	17 1960, 1980, 1987, 1993, 1998, **2003**, 2007, 2008, 2009, 2010, 2011, 2012, 2014, 2015, 2016, 2019, 2020	26 1959, 1962, 1963, 1966, 1968, 1969, 1971, 1974, 1975, 1977, 1978, 1981, 1982, 1984, 1985, 1986, 1990, 1991, 1995, 1997, 2000, 2001, 2002, 2004, 2005, 2006	19 1961, 1964, 1965, 1967, 1970, 1972, **1973**, 1976, 1979, 1983, **1988**, **1989**, 1992, 1994, 1996, **1999**, 2013, **2017**, 2018
	NAO	**–**	**0**	**+**
	van den Dool et al. (2000)	16 **1962**, 1963, 1980, 1987, 1993, **1998**, 2007, 2008, 2009, 2010, 2011, 2012, 2014, 2015, **2016**, 2019	30 **1960**, 1965, 1966, 1968, 1969, 1971, **1973**, 1974, 1975, **1977**, 1978, 1981, 1982, **1984**, 1985, 1986, 1988, **1989**, 1991, 1995, **1997**, 1999, 2000, 2001, 2003, 2004, 2005, 2006, **2017**, 2020	16 **1959**, 1961, **1964**, 1967, 1970, 1972, 1976, 1979, 1983, **1990**, **1992**, 1994, 1996, 2002, 2013, 2018
	Hurrell et al. (2003)	16 **1960**, 1963, **1977**, 1980, 1987, 1993, **1997**, 2007, 2008, 2009, 2010, 2011, 2012, 2014, 2015, 2019	30 **1959**, **1962**, **1964**, 1965, 1966, 1968, 1969, 1971, 1974, 1975, 1978, 1981, 1982, 1985, 1986, 1988, **1990**, 1991, **1992**, 1995, **1998**, 1999, 2000, 2001, 2003, 2004, 2005, 2006, **2016**, 2020	16 1961, 1967, 1970, 1972, **1973**, 1976, 1979, 1983, **1984**, **1989**, 1994, 1996, 2002, 2013, **2017**, 2018

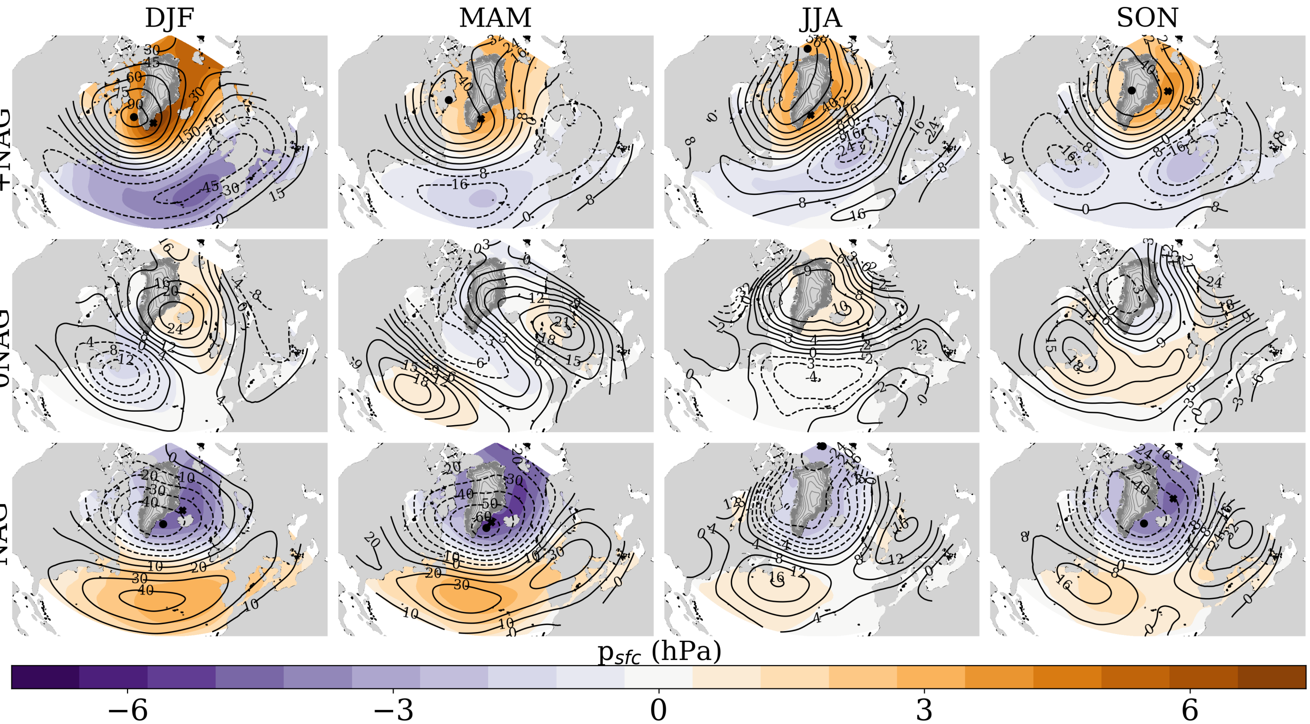

Figure S4. Inter-seasonal 500 hPa geopotential height anomaly (contour lines; positive: solid and negative: dashed; spaced in 10 m intervals), and surface pressure (p_{sfc}) anomaly for each NAG phase with respect to climatology (1959-2000). The ridge (trough) at the surface and at 500 hPa geopotential height anomaly are indicated as dot and cross, respectively, for +NAG (top row) and –NAG (bottom row).

Figure S5 shows the seasonal and spatial integrated surface mass balance according to subsection 2.2, NAG-colored balance (in bars), and the 1991-2020 surface ablation regression.

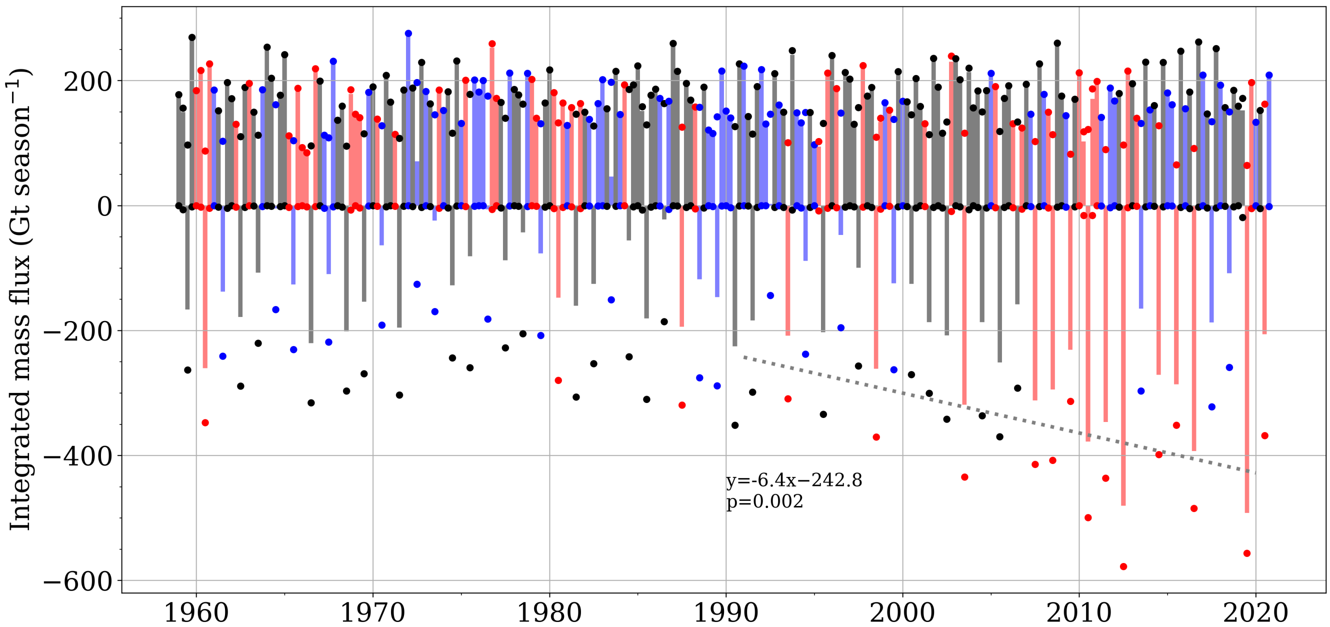

Figure S5. The NAG seasonal and regionally integrated surface mass flux over the GrIS from 1959 until 2020 from RACMO2. North Atlantic influence on Greenland (NAG) is color-coded according to its phase (positive: red; negative: blue; neutral: black). Bubbles (also color-coded based on NAG phase) correspond to seasonal ablation (accumulation) mass flux. Bars (also NAG color-coded) indicate the seasonal surface mass balance. The dotted line is the regression line for summer ablation using T-S slope and the K-T interception between 1991 and 2020 with the associated slope p-value (by the M-K trend test).

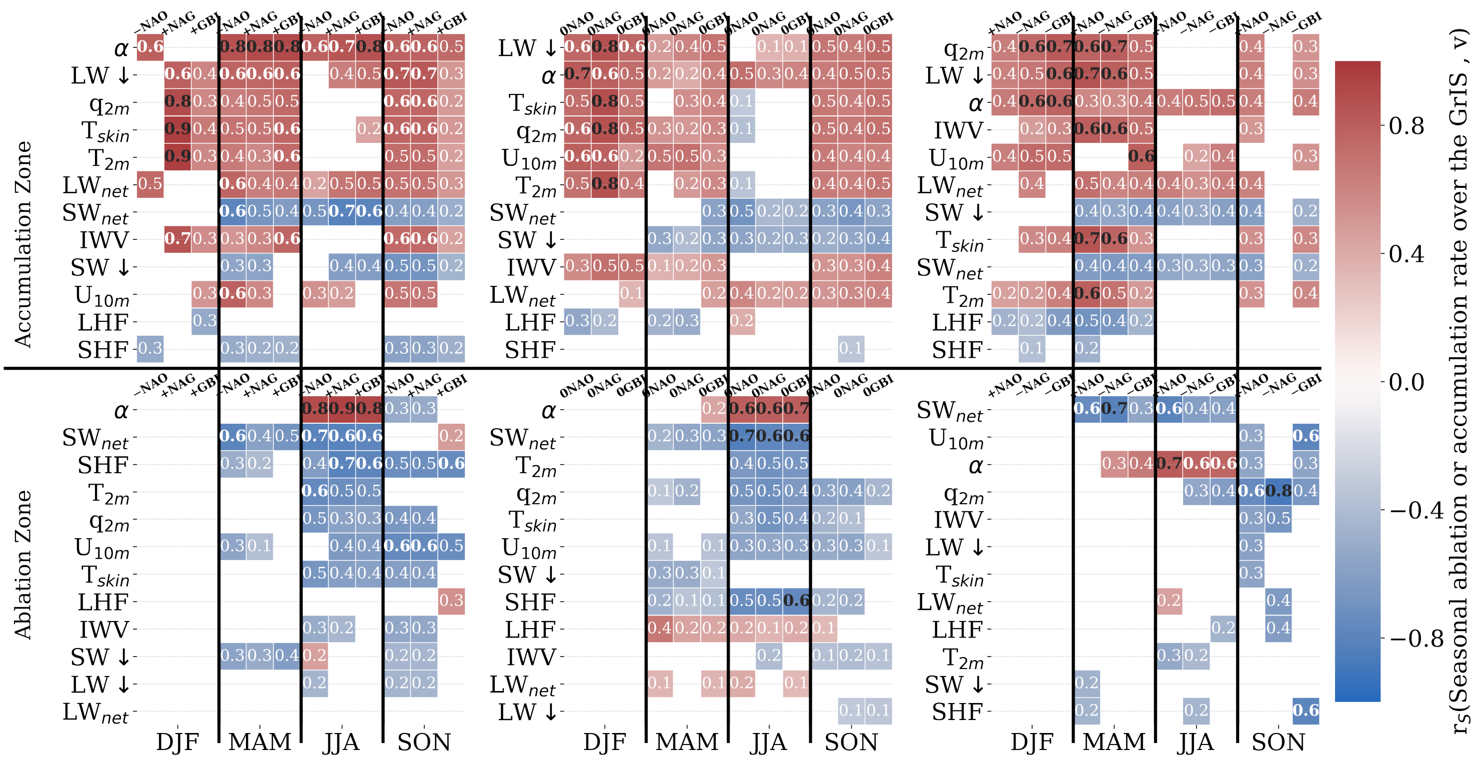

Figure S6. Seasonal correlation matrices between seasonal accumulation (or ablation) rates and atmospheric variables from RACMO2 contributing to the SEB depending on NAO, NAG and GBI phases between 1959 and 2020. The Spearman correlation coefficient is color-coded and the determination coefficient is noted. Correlation matrices are sorted from overall large determination coefficient to small determination coefficient, and highlighted when $r_S^2 \geq 0.6$. Variables were detrended by differencing within clusters.

4 Additional inter-seasonal NAG climatology

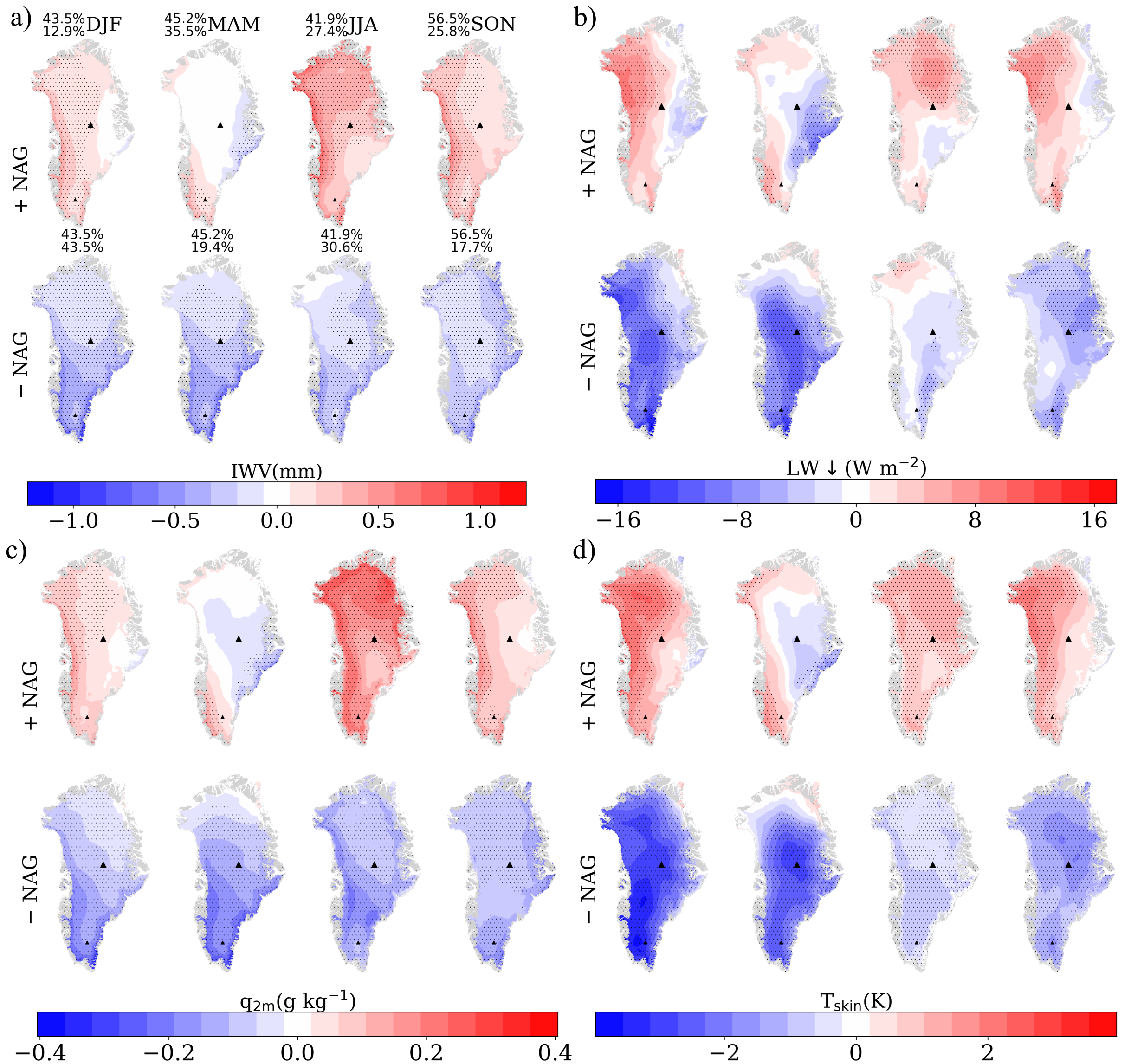

Figure S7. Seasonal and spatial anomalies for (a) integrated water vapor (IWV), (b) incoming longwave radiation at the surface (LW↓), (c) specific humidity at 2m (q_{2m}) and (d) skin temperature (T_{skin}) for opposite NAG phases with respect to the neutral phase ($\overline{+(-)\mathrm{NAG}}$ - $\overline{0\mathrm{NAG}}$) between 1959 and 2020 from RACMO2. The seasonal frequency (f in %) of each NAG phase (+NAG, 0NAG and −NAG) used to produce composites is indicated as subtitle in a). For reference, Summit and South Dome are marked with big and small black triangles, respectively. Stippled regions indicate areas with a confidence level greater than 90% (based on the Wilcoxon rank-sum statistic test for unpaired sets).

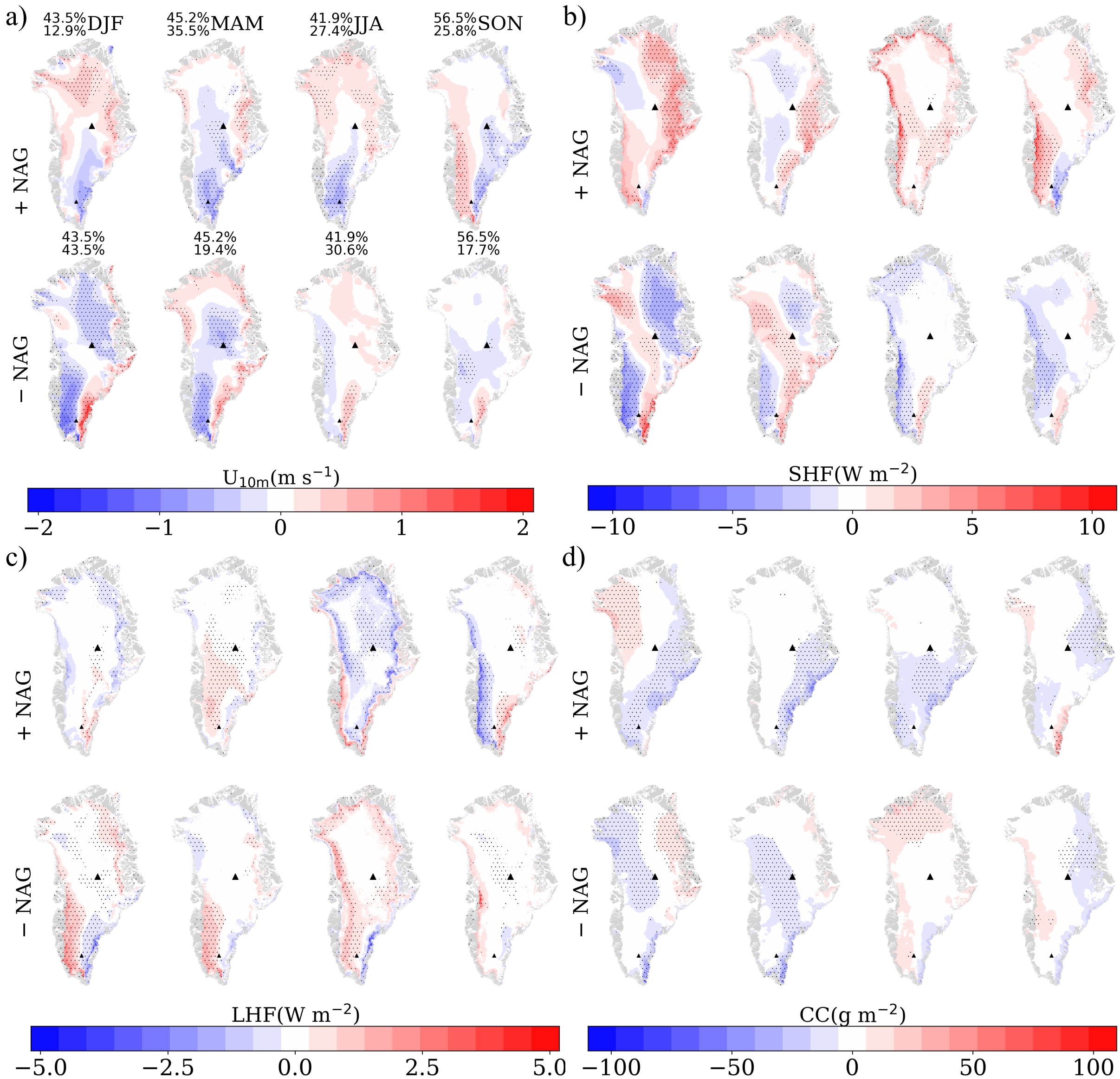

Figure S8. Seasonal and spatial anomalies for (a) near-surface wind speed (U_{10m}), (b) sensible heat flux (SHF), (c) latent heat flux (LHF) and (d) cloud content (CC) for opposite NAG phases with respect to the neutral phase ($\overline{+(-)\mathrm{NAG}}$ - $\overline{0\mathrm{NAG}}$) between 1959 and 2020 from RACMO2. The seasonal frequency (f in %) of each NAG phase (+NAG, 0NAG and −NAG) used to produce composites is indicated as subtitle in Fig. S7a). For reference, Summit and South Dome are marked with big and small black triangles, respectively. Stippled regions indicate areas with a confidence level greater than 90% (based on the Wilcoxon rank-sum statistic test for unpaired sets).

5 NAG, GBI and NAO anomalies

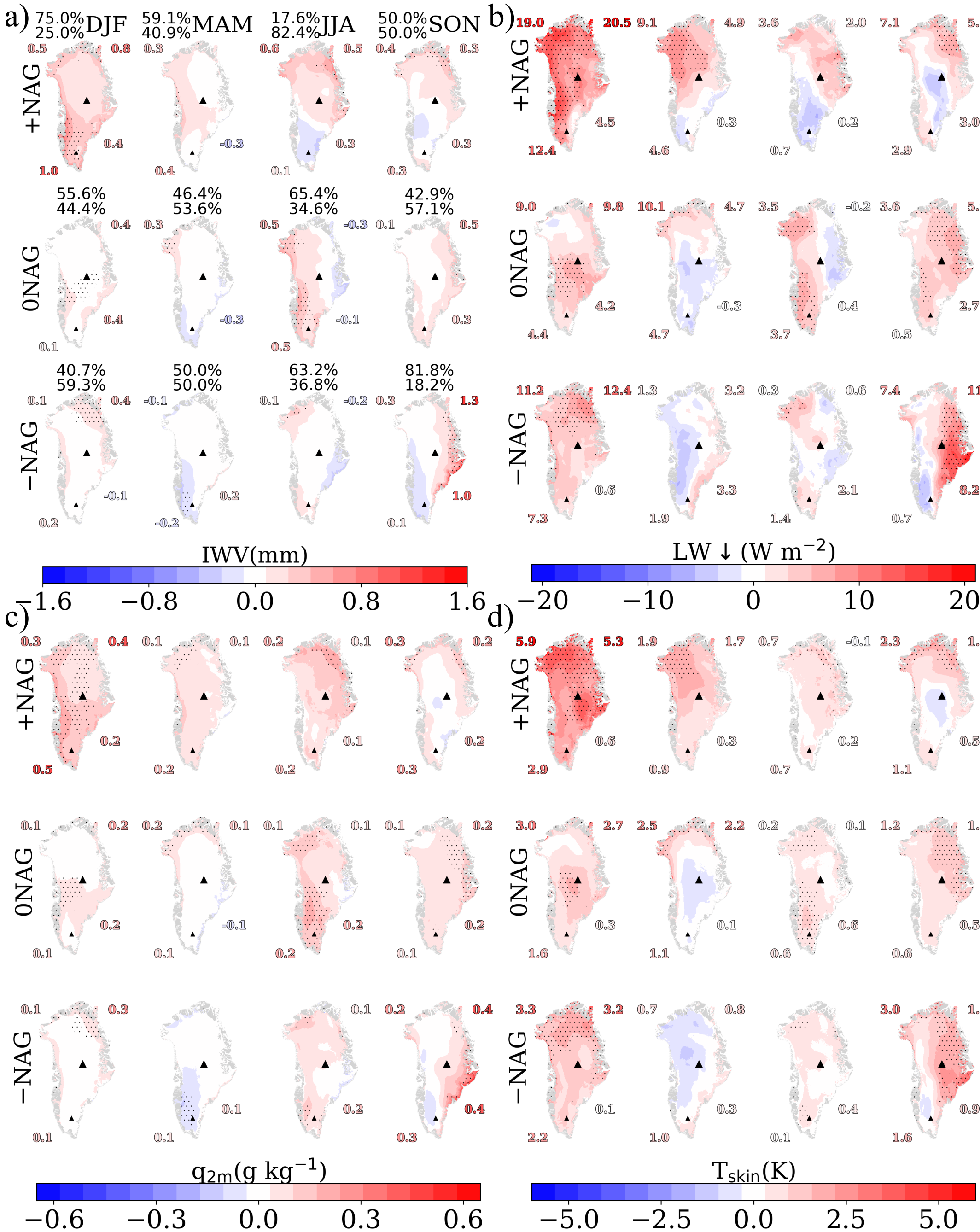

Figure S9. Seasonal and spatial anomalies for (a) integrated water vapor, (b) incoming longwave radiation reaching the surface, (c) near-surface specific humidity, and (d) skin temperature from RACMO2 between 1991-2020 and 1959-1990 as dependent on the NAG phase. The percentage (f) of the NAG phase in each period is indicated for each season. For reference, Summit and South Dome are marked as big and small triangles, respectively. Stippled regions indicate areas with a confidence level greater than 90% (based on the Wilcoxon rank-sum statistic test for unpaired sets). Temporal between composites over the adjacent seas are also shown as colored numbers (Baffin Bay: upper left; Greenland Sea: upper right; Irminger Sea (lower right) and Labrador Sea (lower left). See Figure S1 to discern the extension overseas.

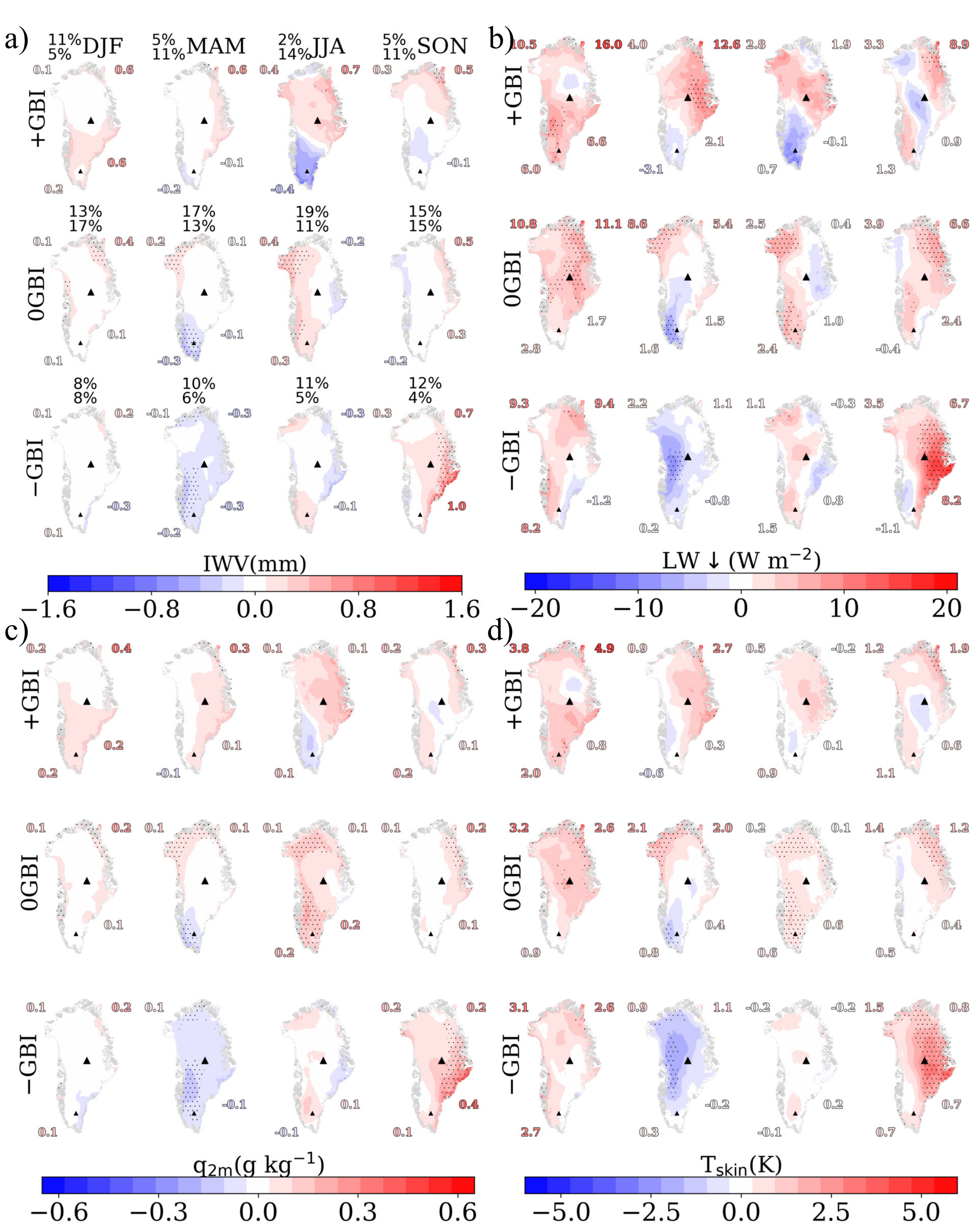

Figure S10. Seasonal and spatial anomalies for (a) integrated water vapor, (b) incoming longwave radiation reaching the surface, (c) near-surface specific humidity, and (d) skin temperature from RACMO2 between 1991-2020 and 1959-1990 as dependent on the GBI phase. The percentage (f) of the GBI phase in each period is indicated for each season. For reference, Summit and South Dome are marked as big and small triangles, respectively. Stippled regions indicate areas with a confidence level greater than 90% (based on the Wilcoxon rank-sum statistic test for unpaired sets). Temporal between composites over the adjacent seas are also shown as colored numbers (Baffin Bay: upper left; Greenland Sea: upper right; Irminger Sea (lower right) and Labrador Sea (lower left). See Figure S1 to discern the extension overseas.

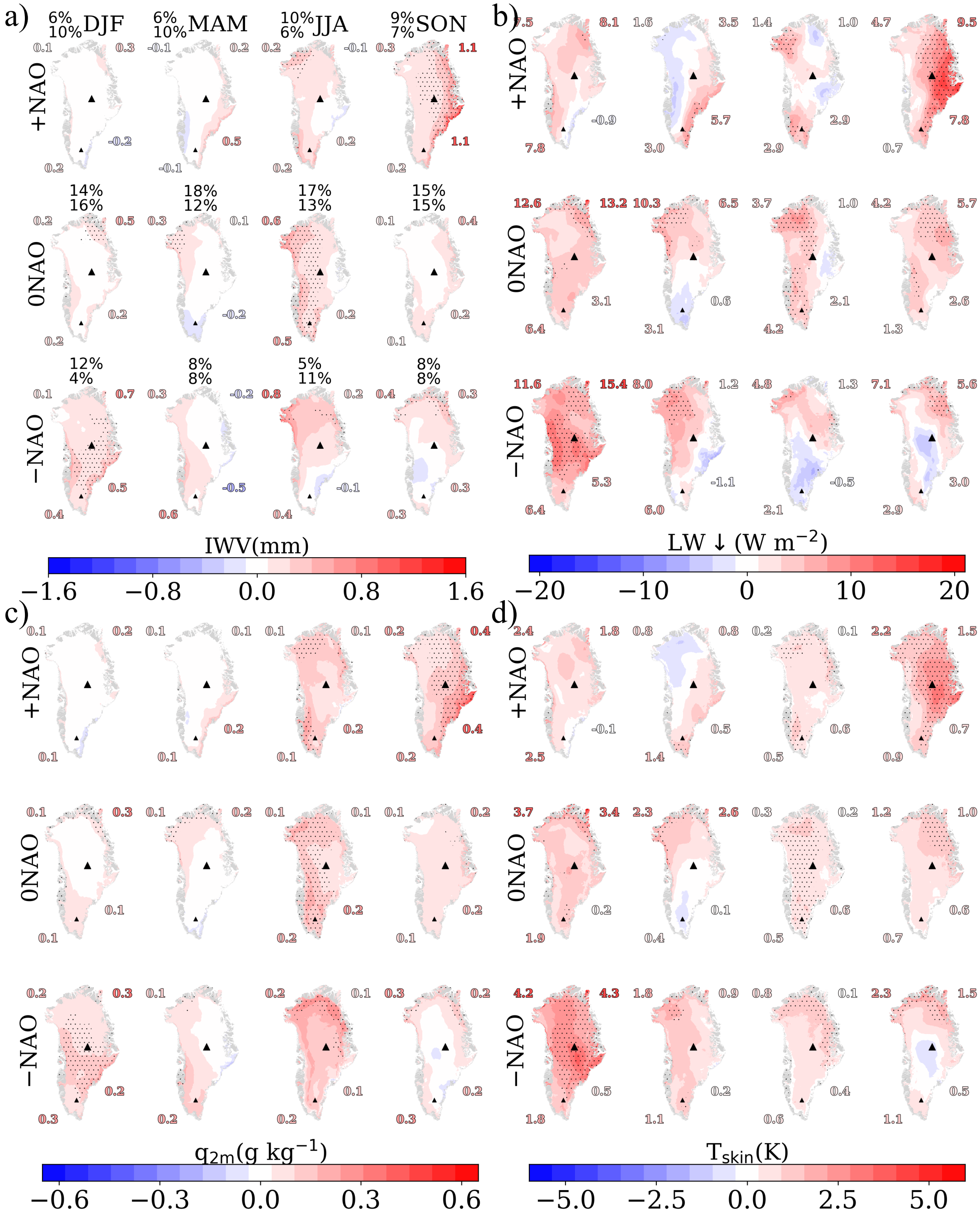

Figure S11. Seasonal and spatial anomalies for (a) integrated water vapor, (b) incoming longwave radiation reaching the surface, (c) near-surface specific humidity, and (d) skin temperature from RACMO2 between 1991-2020 and 1959-1990 as dependent on the NAO phase. The percentage (f) of the NAO phase in each period is indicated for each season. For reference, Summit and South Dome are marked as big and small triangles, respectively. Stippled regions indicate areas with a confidence level greater than 90% (based on the Wilcoxon rank-sum statistic test for unpaired sets). Temporal between composites over the adjacent seas are also shown as colored numbers (Baffin Bay: upper left; Greenland Sea: upper right; Irminger Sea (lower right) and Labrador Sea (lower left). See Figure S1 to discern the extension overseas.

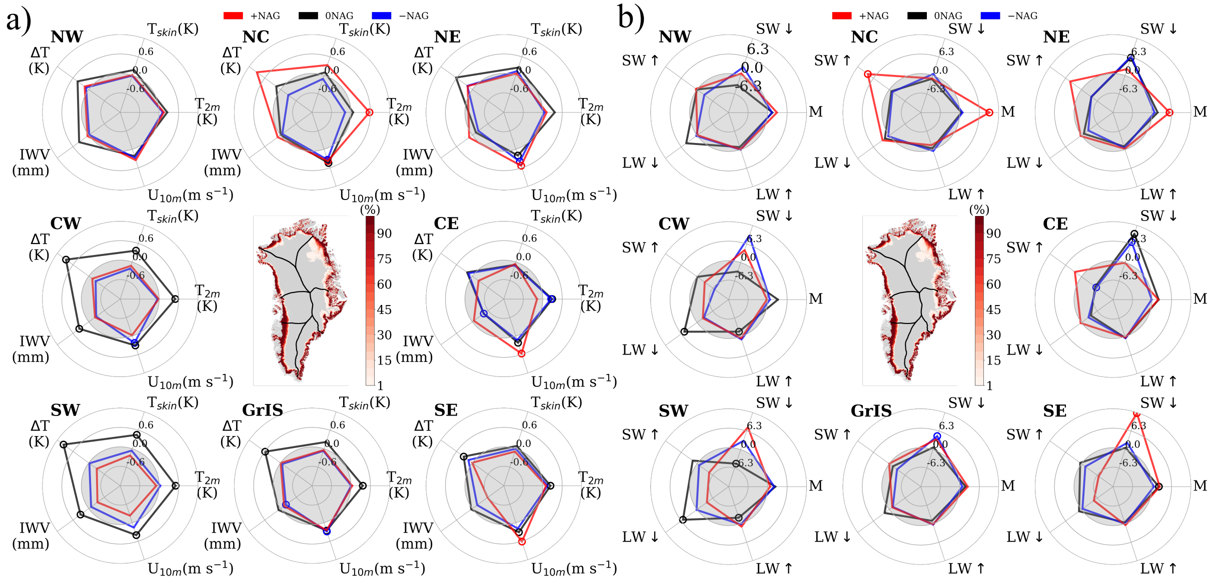

Figure S12. Changes in atmospheric variables contributing to SEB components between 1959-1990 and 1991-2020 in the summer ablation zone for each NAG phase (color-coded). Variables in the panel a) exhibit the variable name and the respective unit. All variables in the panel b) are fluxes in W m $^{-2}$. The spatial relative frequency of ablation is shown at the center. Negative changes are limited by the gray area. Hollow circles indicate significant mean differences based on the Wilcoxon rank-sum statistic test for unpaired sets with a confidence higher than 90%.

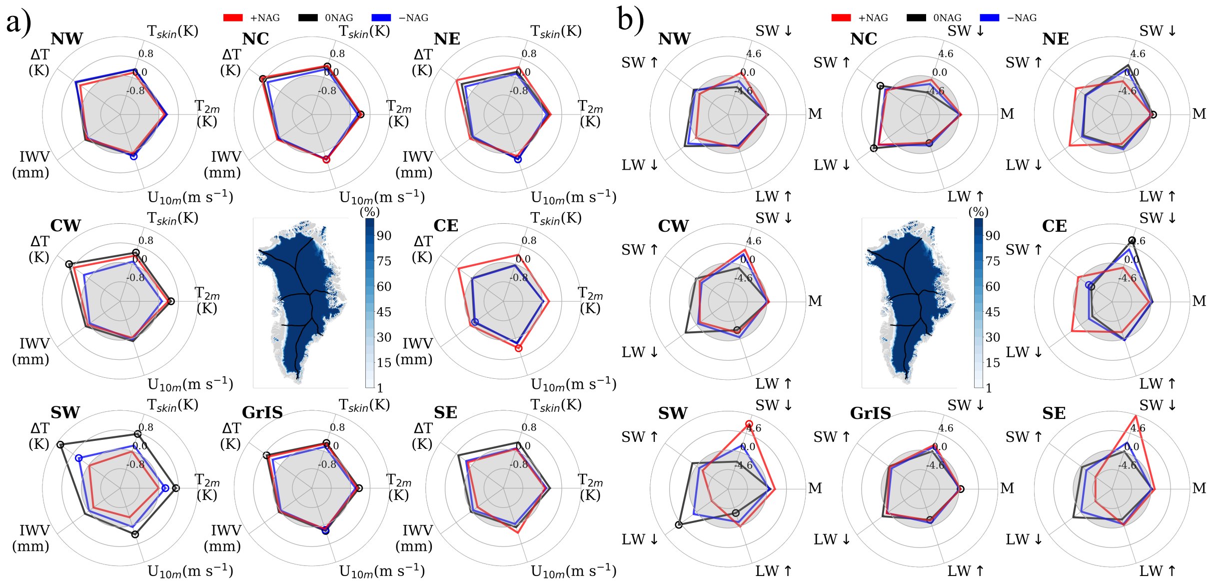

Figure S13. Changes in atmospheric variables contributing to SEB components between 1959-1990 and 1991-2020 in the summer accumulation zone for each NAG phase (color-coded). Variables in the panel a) exhibit the variable name and the respective unit. All variables in the panel b) are fluxes in W m $^{-2}$. The spatial relative frequency of accumulation is shown at the center. Negative changes are limited by the gray area. Hollow circles indicate significant mean differences based on the Wilcoxon rank-sum statistic test for unpaired sets with a confidence higher than 90%.

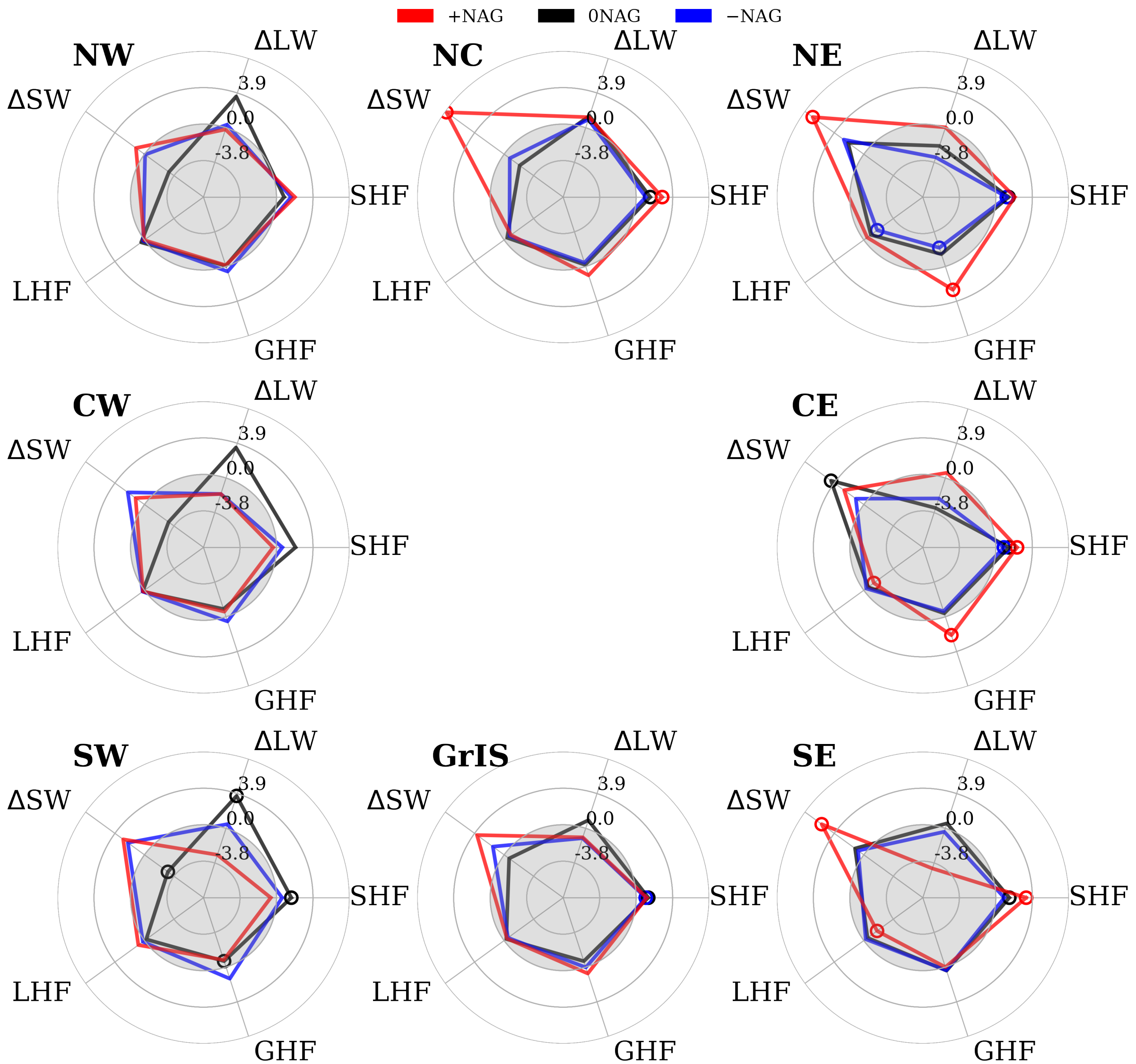

Figure S14. Changes in SEB components between 1959-1990 and 1991-2020 in the summer ablation zone for each NAG phase (color-coded). All variables are fluxes in W m $^{-2}$. Negative changes are limited by the gray area. Hollow circles indicate significant mean differences based on the Wilcoxon rank-sum statistic test for unpaired sets with a confidence higher than 90%. The radar chart supports the analysis of Figure 6.

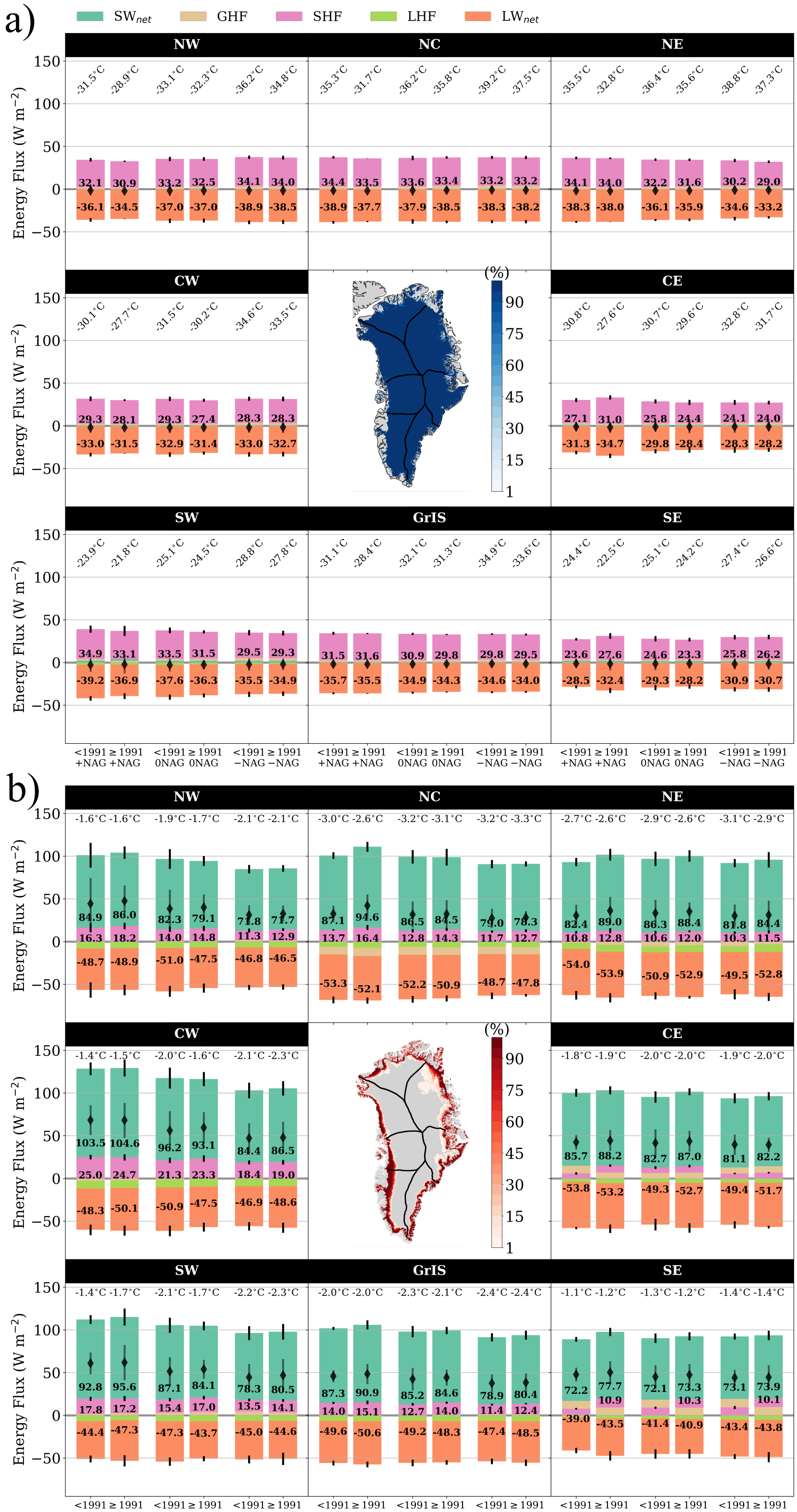

Figure S15. Regional surface energy fluxes before 1991 (<1991) and after (≥1991) in the winter accumulation zone (a) and summer ablation zone for each NAG phase. Areal accumulation (a) and ablation (b) zone contributing to regional averages is shown at the center as relative frequencies.

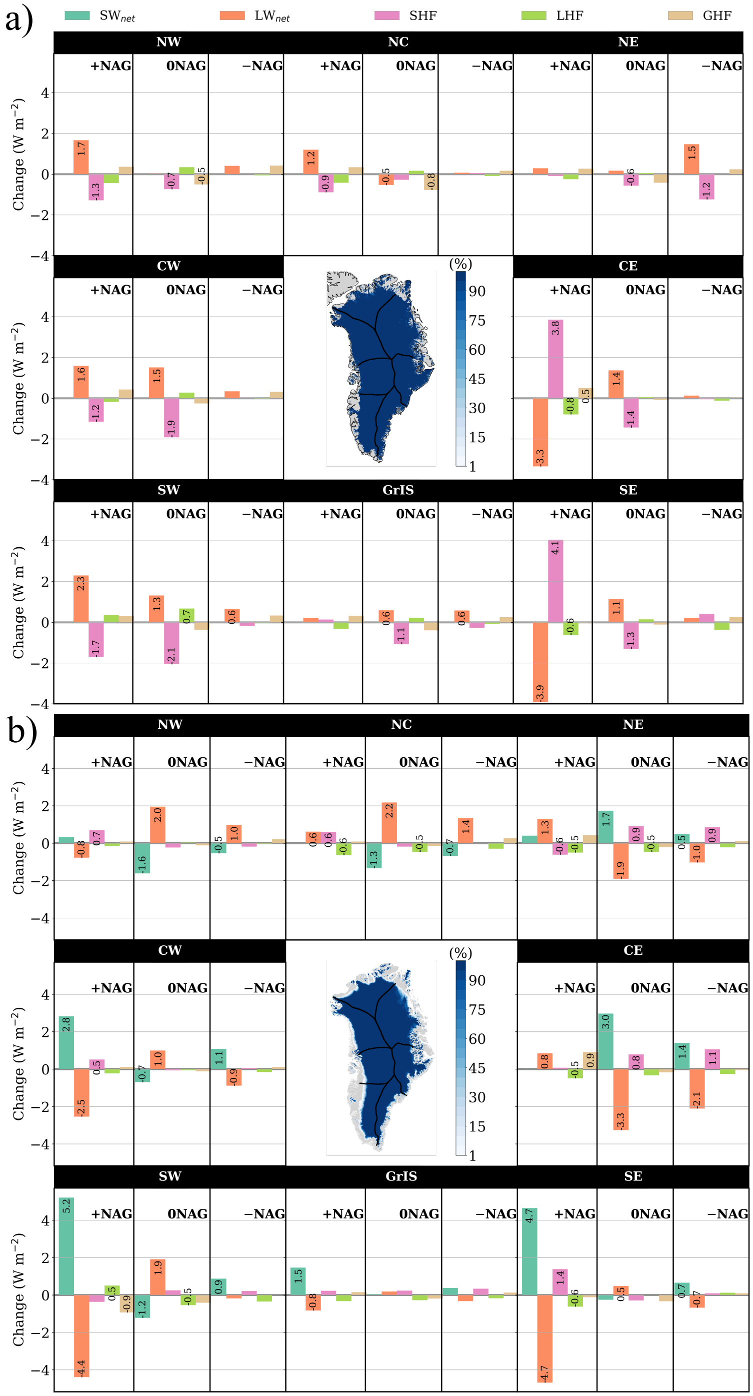

Figure S16. Changes in surface energy fluxes in the winter (a) and summer (b) accumulation zone for each NAG phase. Areal accumulation zone contributing to regional averages is shown at the center as relative frequencies.

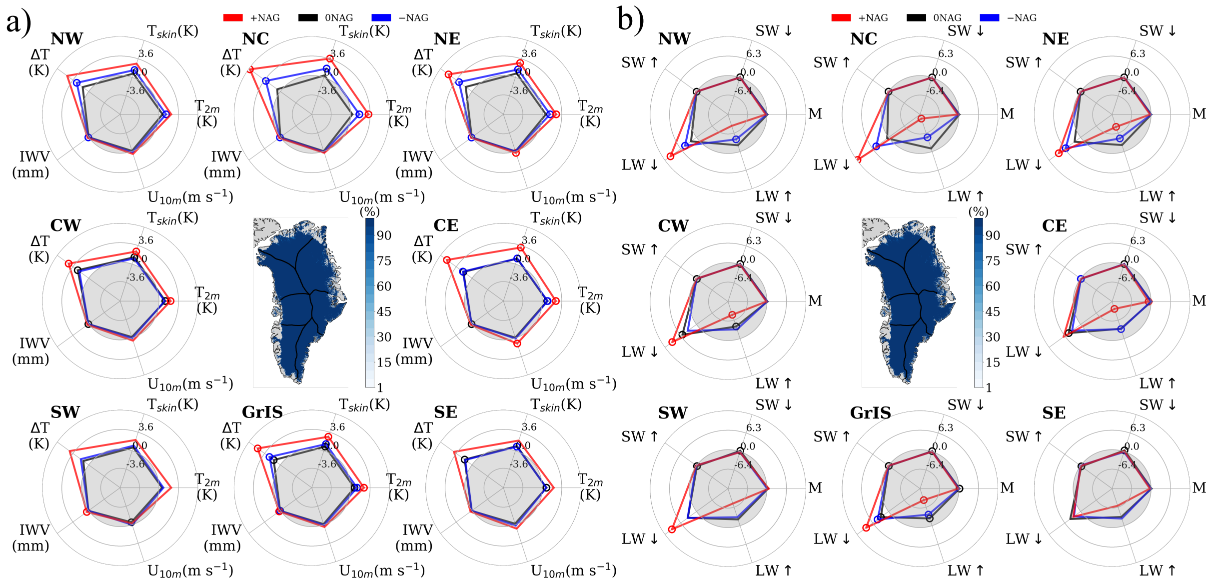

Figure S17. Changes in atmospheric variables influencing SEB components in the winter accumulation zone for each NAG phase. The spatial relative frequency of accumulation is shown at the center. Negative changes are limited by the gray area. Hollow circles indicate significant mean differences based on the Wilcoxon rank-sum statistic test for unpaired sets with a confidence higher than 90%.

References

Hanna, E., Hall, R. J., Cropper, T. E., Ballinger, T. J., Wake, L., Mote, T., and Cappelen, J.: Greenland blocking index daily series 1851–2015: Analysis of changes in extremes and links with North Atlantic and UK climate variability and change, International Journal of Climatology, 38, 3546–3564, https://doi.org/10.1002/joc.5516, 2018.

Hurrell, J. W., Kushnir, Y., Ottersen, G., and Visbeck, M.: An overview of the North Atlantic oscillation, Geophysical Monograph-American Geophysical Union, 134, 1–36, https://doi.org/10.1029/134GM01, 2003.

van den Dool, H., Saha, S., and Johansson, A.: Empirical orthogonal teleconnections, Journal of Climate, 13, 1421–1435, https://doi.org/10.1175/1520-0442(2000)013<1421:EOT>2.0.CO;2, 2000.